Supporting Information for:

Oxygen Vacancy-Enhanced Photothermal Performance and Reactive Oxygen Species Generation for Synergistic Tumour Therapy

Chengjia Peng,[a,‡] Jingju Liu,[a,‡] Liping Guo,[a] Jing Bai,*[a] and Ming Zhou*[a]

[a] *Key Laboratory of Polyoxometalate Science of Ministry of Education, National & Local United Engineering Laboratory for Power Batteries, Key Laboratory of Nanobiosensing and Nanobioanalysis at Universities of Jilin Province, Department of Chemistry, Northeast Normal University, Changchun, Jilin Province 130024, P.R. China*

[‡] These authors contributed equally to this work.

*Corresponding authors: baij243@nenu.edu.cn (J.B.), zhoum739@nenu.edu.cn (M.Z.)

Materials and methods

Chemicals and reagents

Potassium permanganate ($KMnO_4$), gold (III) chloride trihydrate ($HAuCl_4 \cdot 3H_2O$), dimethyl sulfoxide (DMSO, 99%), $[Ru(dpp)_3]Cl_2$ (RDPP), benzoquinone (BQ), 3, 3′, 5, 5′-tetramethylbenzidine (TMB, 99%), 5, 5'-dithiobis-(2-nitrobenzoic acid) (DTNB) and polyvinylpyrrolidone (PVP, Mw~40000) were obtained from Aladdin Reagent Co., Ltd. (Shanghai, China). Trypsin (0.25%, w/v), apenicillin-streptomycin (100×), Dulbecco's modified Eagle's medium (DMEM) and 3-(4, 5-dimethylthiazol-2-yl)-2, 5-dipheny-ltetrazolium bromide bromide (MTT) were purchased from Dingguo reagent Co. (Beijing, China), and passed through a filter of 220 nm before use. 2-(N-morpholino) ethanesulfonic acid (MES) and hydrogen peroxide (H_2O_2, 30%) was purchased from Macklin Biochemical Co., Ltd. (Shanghai, China). Calcein acetoxymethyl ester (calcein AM), 2',7'-dichlorofluorescein diacetate (DCFH-DA), propidium iodide (PI) and fetal bovine serum (FBS) were purchased from Sigma-Aldrich (Shanghai, China). 5, 5', 6, 6'-tetrachloro-1 , 1', 3, 3'-tetraethylbenzimidazolylcarbocyanine iodide (JC-1) staining kit, glutathione (GSH) assay kit and ATP assay kit were purchased from Beyotime Inst. Biotech. (Haimen, China). Other reagents were all purchased from Beijing Chemicals Co. (Beijing, China) and used as received without any purification. Human cervical carcinoma cell lines were obtained from Jilin University Experimental Animal Center (Changchun, China). Ultrapure water (18.2 MΩ) was used throughout the experiments.

Characterization

X-ray diffraction (XRD) analysis was characterized on a Smartlab 9 kW diffractometer (Cu-Kα radiation). X-ray photoelectron spectroscopy (XPS) was measured by an X-ray photoelectron spectrometer (ESCALAB 250). A Cary 50 UV-Vis spectrometer (Varian, USA) was used to measure UV−vis absorption spectra. The UV−vis diffuse reflectance spectrometry (DRS) spectra were measured for the dry-pressed disk samples using a Cary 7000 UV-Vis spectrometer (Varian, USA) in the range of 200–800 nm at room temperature. Transmission electron microscope (TEM) images and element mapping were taken by a transmission electron microscope with 200 kV voltage (JEOL-2100F, Tokyo, Japan). A Nicolet 6700 spectrometer (Nicolet, USA) was used to record fourier transform infrared (FTIR) spectra. Electron spin resonance (ESR) spectroscopy was performed on a Bruker E500 spectrometer. The photoluminescence (PL) spectra were obtained on a fluorescence spectrophotometer (FLSP-920, Edinburgh Instruments) with an excitation laser at 270 nm. The hydrodynamic sizes and zeta potentials of materials were measured using a Zetasizer Nano ZS (Malvern, UK).

Synthesis of MnO₂@Au NCs

The MnO₂@Au NCs were firstly synthesized through a facile one-step reduction process. In brief, KMnO₄ (7.9 mg), MES (213 mg), HAuCl₄·3H₂O (17 mg) and PVP (Mw~40000, 100 mg) were dissolved into 20 mL of deionized water and sonicated (300 W) for 1 h. Then, the reaction mixture was centrifuged and washed several times using ultrapure water for removing excessive reagents. Finally, the dark grown products were obtained and denoted as MnO₂@Au NCs. As controls, the pure MnO₂ nanosheets (MnO₂ NSs) were also obtained according to above-mentioned procedures except for the addition of gold precursors.

***In vitro* evaluation of GSH Level and O₂ generation**

To investigate the GSH-depleting capability of MnO₂-based nanomaterials, DTNB was employed as a detection probe to evaluate the GSH level. Briefly, a GSH aqueous solution (10 mM) was incubated with or without pure MnO₂, MnO₂@Au or MnO₂@Au/L (100 μg/mL, 10 mL) for 30 min under stirring. Then, DTNB solution (10 μL, 20 mg/mL) was added into above-mentioned supernatant after incubation for another 30 min. Finally, the GSH level was measured by detecting the absorption of 410 nm.

The oxygen production from H₂O₂ splitting by MnO₂-based nanomaterials was monitored using a dissolved oxygen meter (JPBJ-608, Leici, China). In brief, an oxygen probe is inserted into the 30 mL of PBS solution (pH 6.0) containing 100 μM of H₂O₂ and Au (3.43 μg/mL), MnO₂ (100 μg/mL) or MnO₂@Au (100 μg/mL, 3.43 μg/mL of Au) with or without laser irradiation, and H₂O₂ (100 μM) alone was served as control. Then, the oxygen amount was monitored for 10 min.

***In vitro* photothermal measurement**

To evaluate the photothermal performance of materials, 1 mL test solutions of PBS, Au (3.43 μg/mL), MnO₂ (100 μg/mL), and MnO₂@Au (100 μg/mL, 3.43 μg/mL of Au) or different concentrations of MnO₂@Au (50-200 μg/mL) were irradiated under a laser of 808 nm (1.0 W/cm²) for 10 min. The 100 μg/mL of MnO₂@Au solution was irradiated under an 808 nm laser at different power densities (0.5, 1.0, 1.5, 2.0 and 2.5 W/cm²) for 10 min to determine the impact of laser power intensity. To determine the photostability, 100 μg/mL of MnO₂@Au solution was repeatedly exposed to an 808 nm laser for five on/off cycles. The temperature and photothermal images were recorded every 30 s by an infrared thermal imager (FLIR E50, Inc., USA).

Reactive oxygen species detection

The ·O$_2^-$ generation was measured by a colorimetric method based on TMB oxidation. For detecting ·O$_2^-$, 50 µL test solutions of Au (68.6 µg/mL), MnO$_2$ (2.0 mg/mL) or MnO$_2$@Au (2.0 mg/mL, 68.6 µg/mL of Au) were mixed with 10 µL of TMB (50 mM) in a buffer solution (1 mL, pH 4.0). Also, to evaluate the enhancement of ·O$_2^-$ generation from heat during PTT, the MnO$_2$@Au/TMB mixture was irradiated under an 808 nm laser (1.0 W/cm^2) for 10 min. And different power density of laser were used to irradiate MnO$_2$@Au/TMB mixture for determining the impact of laser power for ·O$_2^-$ generation, the mixture was irradiated under 808 nm laser at for 10 min, and the absorbance at 650 nm was measured.

Computational method

The structural parameters of δ-MnO$_2$ is determined by XRD (space group: R3-M, a = b = 2.868 Å, c = 19.202 Å, α=β=γ=90º). The supercell of δ-MnO$_2$ was 3×3×1 in the a-, b-, and c- directions. Plane-wave density functional theory (DFT) + U calculations of δ-MnO$_2$ were carried out using the CASTEP module. LDA/GGA was used for the DFT exchange correlation energy. A Hubbard type potential was introduced to treat the strongly correlated compound (LDA + U). According to the existing Literature, the value of U was set as 2.5 eV for Mn 3d states.[1] The cutoff energy of plane-wave basis was set to 400 eV. The Brillouin zone was sampled with 3×3×4 k-points. According to previous study, δ-MnO$_2$ exposures the most stable crystal (001) surface.[2] Thus the (001) surfaces of δ-MnO$_2$ were modeled with vacuum space of 15 Å to calculate adsorption energy. The equation for computing the adsorption energies of O$_2$ on δ-MnO$_2$ (001) surface was as follows:

$$E_{ads} = E_{MnO_2/O_2} - (E_{MO_2} + E_{O_2})$$

E_{MnO_2/O_2} is the total energy of the O$_2$ adsorbed δ-MnO$_2$. E_{MnO_2} and E_{O_2} is the total energy of the δ-MnO$_2$ and E_{O_2}.

Cell culture and cytotoxicity

HeLa cells (cervical cancer cell lines) were grown in high glucose DMEM containing 10% fetal bovine serum and 1% penicillin/streptomycin under standard conditions (37 °C, 5% CO$_2$). When cell growth reaches 80% confluence, 0.25% of trypsin (w/v) was used to digest cells. Then cells were resuspended in DMEM medium and used for passaging or plating.

Cell cytotoxicity was measured through a standard MTT method. The HeLa cells (1×10^4 cells/well) were grew in 96-well plate until 80% of confluence. After removing culture medium, cells were further incubated in DMEM with a series of concentrations (0-200 µg/mL) of MnO_2, MnO_2@Au (OT), MnO_2@Au/BQ with laser irradiation (MnO_2@Au/BQ/L, PTT) or MnO_2@Au with laser irradiation (MnO_2@Au/L, PTT/OT) for another 24 h. For irradiation group, each well was irradiated with an 808 nm laser (1.0 W/cm^2) for 10 min. Then, 100 µL of MTT solution (0.5 mg/mL) was added for another 4 h. Finally, the generated blue formazan was dissolved in DMSO, and cell viability was evaluated by measuring the absorbance at 550 nm on a Synergy H1 microplate reader (BioTek, USA). Normalized absorbance of experiment groups by extracting the control was used to express the cell viability.

The synergistic therapeutic effects of MnO_2@Au towards HeLa cells were further explored by live/dead cell staining assay. HeLa cells in culture plate with 1×10^5 cells/mL were incubated with fresh DMEM, only laser, MnO_2, MnO_2@Au, MnO_2@Au/BQ/L and MnO_2@Au/L for 24 h, respectively. Then, the cells were costained by 0.1 µM of calcein-AM and 4 µM of PI solution for 30 min. Fluorescence images were observed *via* confocal laser scanning microscopy (CLSM, FV1000, Olympus, Japan).

Intracellular ROS generation

For intracellular $\cdot O_2^-$ detection, HeLa cells (1×10^5 cells/mL) were seeded in culture disk (20 mm) and exposed to DMEM, MnO_2 (100 µg/mL) and MnO_2@Au (100 µg/mL) with or without laser irradiation for 24 h. For irradiation group, each dish was irradiated with NIR laser (808 nm, 1.0 W/cm^2) for 10 min. Then, the cells were stained by 10 µM of DCFH-DA for 0.5 h, followed by imaging *via* CLSM with excitation wavelength of 488 nm.

Evaluation of mitochondrial membrane potential (MMP)

For MMP detection, HeLa cells (1×10^5 cells/mL) were cultured in fresh DMEM with or without laser irradiation, MnO_2 (100 µg/mL), MnO_2@Au (100 µg/mL), MnO_2@Au/BQ/L (100 µg/mL of MnO_2@Au, 100 µg/mL of BQ) or MnO_2@Au/L (100 µg/mL) for 24 h, respectively. For irradiation group, each dish was irradiated with a NIR laser (808 nm, 1.0 W/cm^2) for 10 min. Then, the cells were stained with 3 µg/mL of JC-1 for 30 min followed by cold JC-1 buffer solution rinsing. Finally, the MMP was observed by CLSM with red channel for J-aggregates (high MMP) and green channel for JC-1 monomer (low MMP), respectively.

Intracellular ATP level

The HeLa cells (1×10^5 cells/mL) were seeded in culture disk for overnight, and then the cells were exposed to DMEM with or without laser irradiation, MnO_2 (100 μg/mL), $MnO_2@Au$ (100 μg/mL), $MnO_2@Au/BQ/L$ (100 μg/mL of $MnO_2@Au$, 100 μg/mL of BQ) or $MnO_2@Au/L$ (100 μg/mL) for another 24 h, respectively. For irradiation group, each well was irradiated with a NIR laser (808 nm, 1.0 W/cm^2) for 10 min. Afterwards, the cells were collected and lysed using a lysis solution on an ice bath for 3 h, followed by centrifugation (5 min, 12000 rpm). Finally, 500 μL of cell supernatant was mixed with ATP test solution (1.0 mL) for 30 min. Finally, the intracellular ATP level was quantified by detecting luminescence of supernatant using a microplate reader.

Measurement of intracellular GSH level and O$_2$ generation

GSH assay kits were used to detect the intracellular GSH level by UV-vis. To investigate intracellular GSH depletion, HeLa cells were incubated by DMEM with or without MnO_2 (100 μg/mL), $MnO_2@Au$ (100 μg/mL) or $MnO_2@Au/L$ (100 μg/mL) for 24 h. Then, the cells were collected and lysed using a lysis solution on an ice bath for 3 h. After lysis, 500 μL of cell supernatant was mixed with 1.0 mL of test solutions for 30 min. Finally, the intracellular GSH level was quantified by detecting the absorption of reaction solution at 410 nm.

The intracellular O$_2$ was quantified using the fluorescence probe of RDPP, whose fluorescence could be significantly quenched resulting from oxygen presence. Briefly, HeLa cells were treated with 10 μM of RDPP for 4 h, and then exposed to DMEM with or without MnO_2 (50 μg/mL), $MnO_2@Au$ (50 μg/mL) or $MnO_2@Au/L$ (50 μg/mL) for another 6 h and washed twice with PBS. Afterwards the fluorescence of RDPP was observed by a CLSM with 488 nm excitation wavelength.

Establishment of tumour animal models

Kunming female mice (18-21 g, 5-7 weeks) were purchased from Experimental Animal Center of Jilin University (China). Animal protocol has been approved by the Experimental Animal Care and Use Committee of Jilin University (Permit number: 201907005). To establish U14 tumour models, each mouse was injected subcutaneously 150 μL of U14 cells suspension (1.5×10^5 cells/mL). A week later, the tumour volume grew to ~100 mm^3, and *in vivo* experiments were then carried out.

***In vivo* pharmacokinetic, biodistribution and photothermal imaging of MnO$_2$@Au NCs**

For pharmacokinetic analysis, tumour-bearing mice were intravenously administered 800 μL of $MnO_2@Au$ NCs (100 μg/mL). Then, the blood of mice (200 μL) were collected at a given time point (15 min, 30 min, 1 h, 2 h, 4 h, 12 h, and 24 h) and dissolved in nitric acid. To study the biodistribution of $MnO_2@Au$ NCs, the tumours and major organs (spleen, kidney, lung, heart and

liver) were extracted and digested with nitric acid for 24 h. The Mn contents in the blood and tissues were quantified using an inductively coupled plasma-atomic emission spectroscopy (ICP-AES, Thermo Scientific, USA), and the untreated mice were used as a control.

For *in vivo* thermal imaging, 800 μL of saline, Au NPs (3.43 μg/mL), MnO_2 (100 μg/mL) or $MnO_2@Au$ (100 μg/mL, 3.43 μg/mL of Au) were intravenously injected into mice. After 24 h, tumours were irradiated by an 808 nm laser (1.0 W/cm^2) for 10 min, meanwhile the temperature was recorded by an infrared thermal imaging system.

In vivo oxygen vacancy-enhanced PTT and OT

The tumour-bearing mice were randomly assigned into 6 groups (n=10): (i) saline (control group), (ii) only laser irradiation, (iii) MnO_2, (iv) $MnO_2@Au$ (OT group), (v) $MnO_2@Au/BQ$ plus laser irradiation ($MnO_2@Au/BQ/L$, PTT group) and (vi) $MnO_2@Au$ plus laser irradiation ($MnO_2@Au/L$, PTT/OT group). The sample dispersions were intravenously injected every other day. The dose of injection is 800 μL at a concentration of 100 μg/mL, 3.43 μg/mL, 100 μg/mL for MnO_2, Au and BQ, respectively. At 24 h postinjection, the groups ii, v, and vi were irradiated by a NIR laser (808 nm, 1.0 W/cm^2) for 10 min. The lengths and widths of tumours were measured every two days for two weeks, and the tumour volume of the mouse was calculated according to the formula: tumour volume (mm^3) = width^2 × length/2. Body weight of mouse was measured using a balance every two days for assessing the physiological toxicity of materials in treatment process. After two weeks, the mice were sacrificed under CO_2, and tumour tissues in different groups were dissected, weighed and taken photographs. Then, the tumours and main organs (lung, kidney, spleen, heart, and liver) were collected and soaked in 4% formalin overnight. The collected tissues were sectioned to slices and stained using hematoxylin and eosin (H&E). Images were observed by a digital microscope (Leica QWin).

Statistical analysis

A Student's t test statistical analysis was performed to compare two-group differences through. Mean ± standard deviation (SD) through at least three experiments were provided for all data. *p < 0.05 was considered as statistical significance.
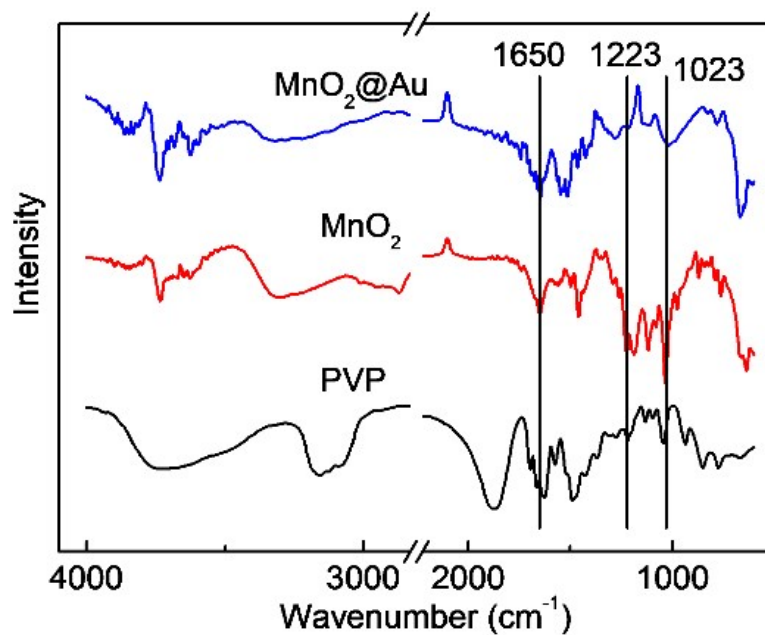
Fig. S1 FTIR spectra of PVP, MnO$_2$ NSs and MnO$_2$@Au NCs.

The PVP as stabilizer to improve colloidal stability of MnO$_2$@Au NCs have been verified by the appearance of the bands at 1650, 1223 and 1023 cm^{-1} for C=O, O=C–N and C–C bonds in the FTIR spectra.
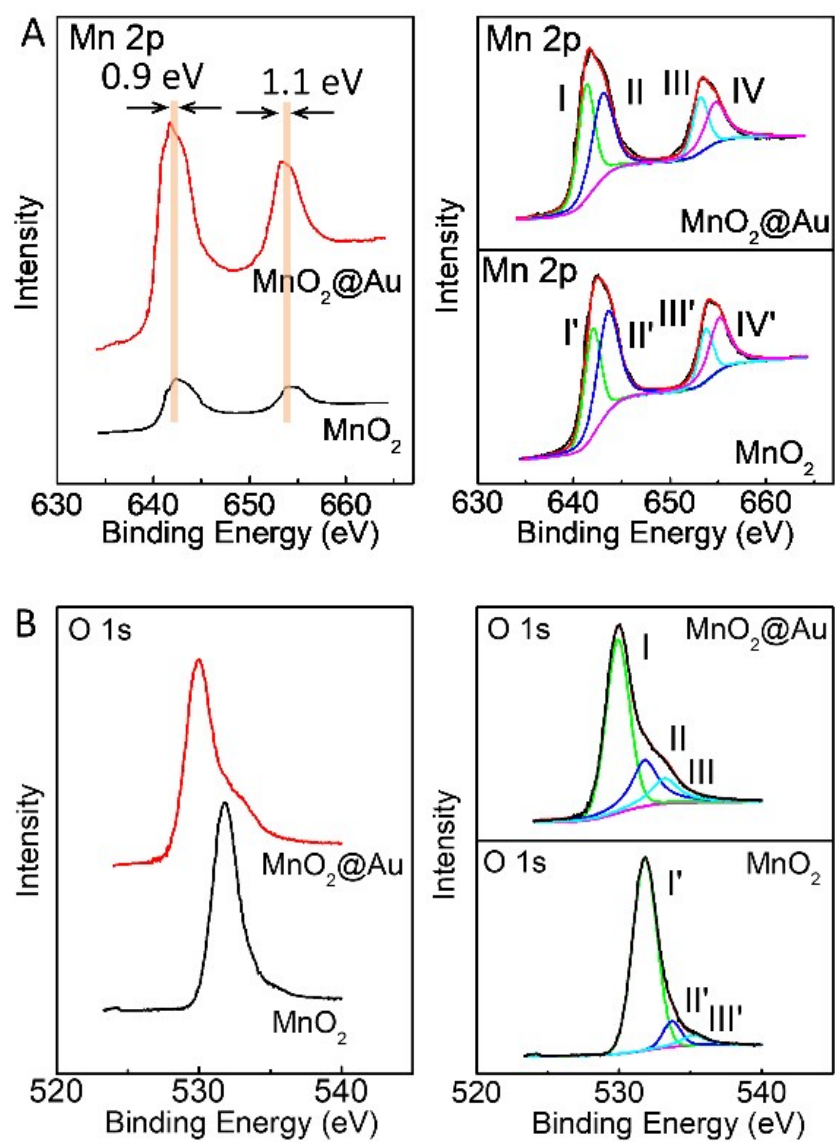
Fig. S2 Mn 2p (A) and O 1s (B) high-resolution XPS spectra of the MnO_2@Au NCs.
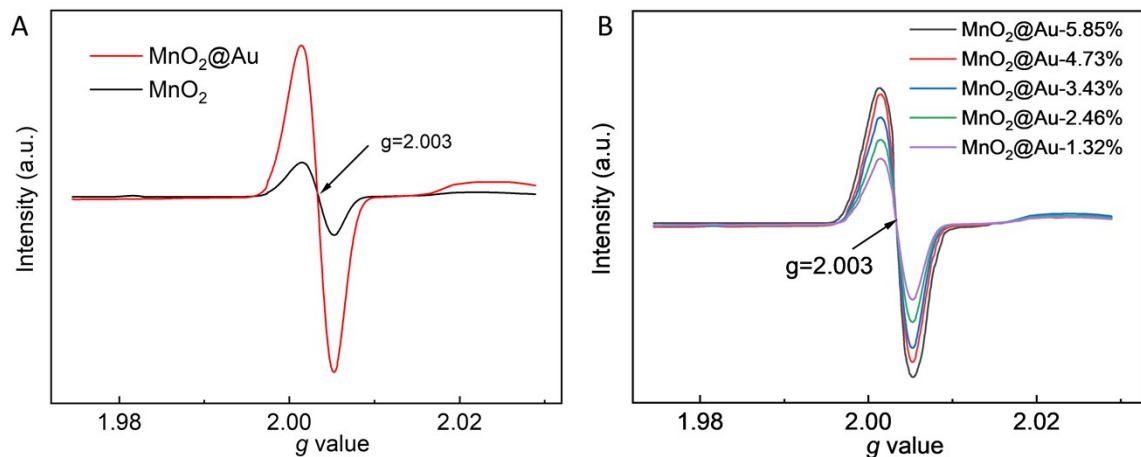
Fig. S3 (A) ESR spectra of MnO_2@Au and MnO_2. (B) ESR spectra of MnO_2@Au with different amount of Au doping.

As shown in Fig. S3A, the ESR spectrum of MnO_2@Au display a detectable O_v signal at a g value of ~2.003, resulting from the Au-doping step. However, a relatively weak peak signal was observed in pure MnO_2, indicating few oxygen vacancies. Thus, one can deduce that there are plenty of oxygen vacancies in the MnO_2@Au nanostructures, which were able to be adjusted by controlling the amount of Au doping during the synthesis process (Fig. S3B).
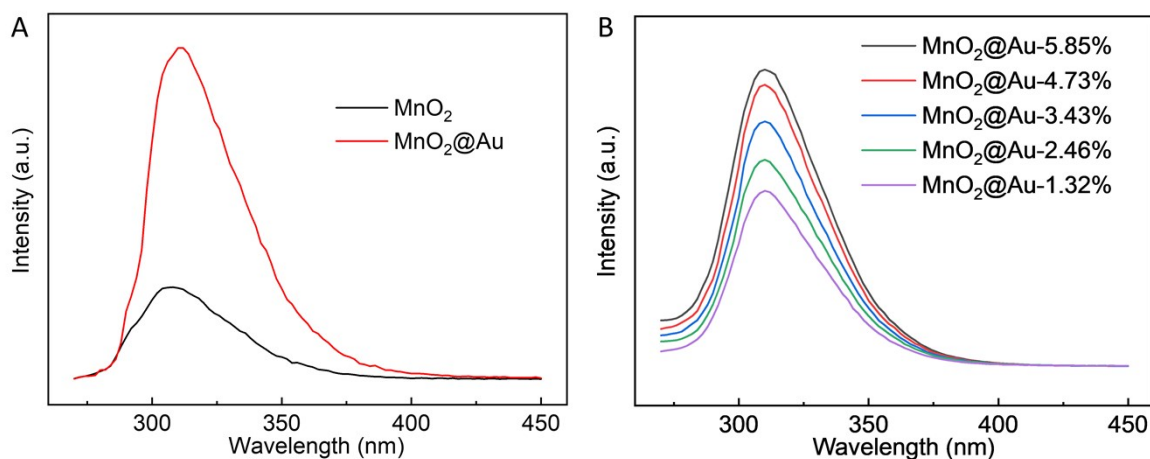
Fig. S4 (A) Photoluminescence (PL) spectra of the MnO_2 and MnO_2@Au. (B) Photoluminescence (PL) spectra of MnO2@Au with different amount of Au doping.

Compared to pure MnO_2, a stronger PL emission peak at 312 nm was observed for the MnO_2@Au (Fig. S4A), which was related to the traps on surface oxygen defects. Especially, with the increase of Au-doping, the oxygen vacancy concentration increases in MnO_2@Au, resulting in increased PL signal (Fig. S4B). However, only a weak peak signal at 312 nm was observed in pure MnO_2. The PL result further supported the existence of oxygen vacancies in MnO_2@Au due to Au doping.
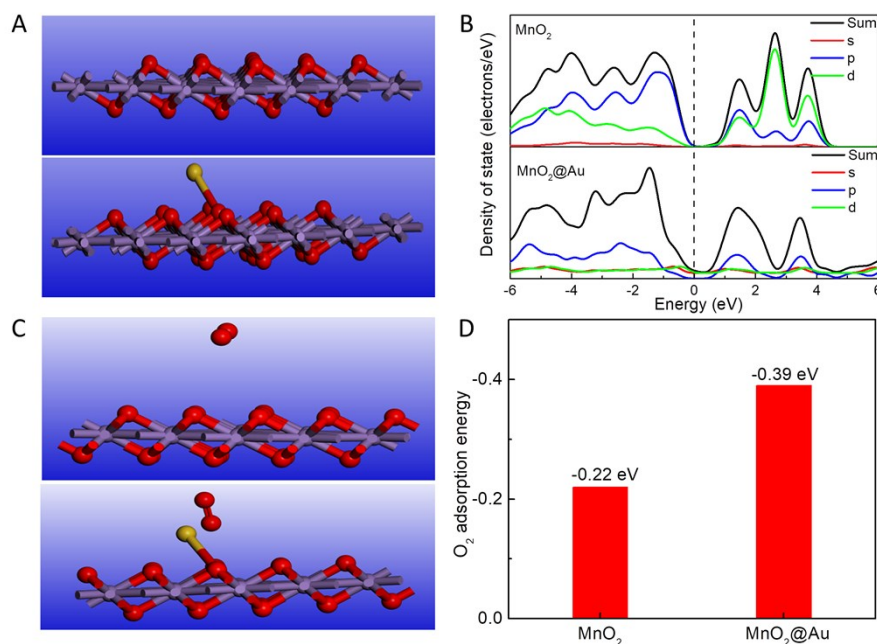
Fig. S5 (A) Schematic crystal structure model of pure MnO_2 and $MnO_2@Au$. (B) Calculated density state of pure MnO_2 and $MnO_2@Au$. (C) The adsorption configurations of the O_2-adsorbed on pure MnO_2 and $MnO_2@Au$. (D) DFT-calculated adsorption energies for O_2 molecules on the surfaces of pure MnO_2 and $MnO_2@Au$. The purple spheres represent Mn atoms, red spheres represent O atoms, and yellow spheres represent Au atoms. The Fermi level (E_F) is set at 0 eV.

Table S1 E_{ads} is adsorption energy of O_2 on the MnO_2 surface (001). D is the closest adsorption distance of O_2 to the surface (001). d_{Mn-O} is Mn-O bond distance near the O_2 molecule. d_{O-O} is the structural parameters of O_2 after optimize.

Configuration	E_{ads} (eV)	D (Å)	d_{Mn-O} (Å)	d_{O-O} (Å)
Free O_2	—	—	—	1.228
Free MnO_2	—	—	1.942	—
O_2/MnO_2	-0.22	3.524	1.942	1.228
$O_2/MnO_2@Au$	-0.39	2.231	1.956	1.226

The first-principles calculations based on density functional theory (DFT) were performed to gain deeper insights about the impact of oxygen-vacancy engineering on electronic properties of $MnO_2@Au$. The optimized geometries for model MnO_2 and $MnO_2@Au$ are displayed in Fig. S5A. Thus, the band structures for both MnO_2 and $MnO_2@Au$ are calculated, respectively. The profiles of

the density of states (DOS) are different before and after Au-doping (Fig.5B). Compared to pure MnO_2, the DOS of $MnO_2@Au$ is continuous near the Fermi level (E_F), confirming the presence of oxygen deficiency. Also, the band gap energy of $MnO_2@Au$ is much lower than that of pure MnO_2, which is agreed with DRS result. Under 808 nm irradiation, an electron located in the HOMO level of $MnO_2@Au$ is excited into the LUMO level. Then, the exciton created recombines *via* nonradiative processes, releasing heat. The introduction of O_v in MnO_2 results in a narrower band gap, which can decrease the activation energy for photo-generated electron−hole recombination. According to the Arrhenius equation, the nonradioactive rate has an inverse exponential relation with the activation energy.[3] Therefore, the narrower band gap derived from the O_v facilitates the photothermal conversion by increasing the nonradiative rate.

The adsorption properties of oxygen molecules can be viewed as an important descriptor to evaluate the interaction between oxygen and catalyst surfaces. Thus, we performed DFT calculations to determine the structure and energy change of O_2 molecules adsorbed on the surface of pure MnO_2 and $MnO_2@Au$ (Table S1). The optimized structure of O_2 absorption was shown in Fig. S5C. The calculated absorption energy of O_2 for $MnO_2@Au$ (-0.39 eV) was lower than -0.22 eV of pure MnO_2. Moreover, the increased the charge density around the valence band of $MnO_2@Au$ enhance O_2 activation. The results indicate the stronger and easier capability of adsorbing O_2 for $\cdot O_2^-$ generation.
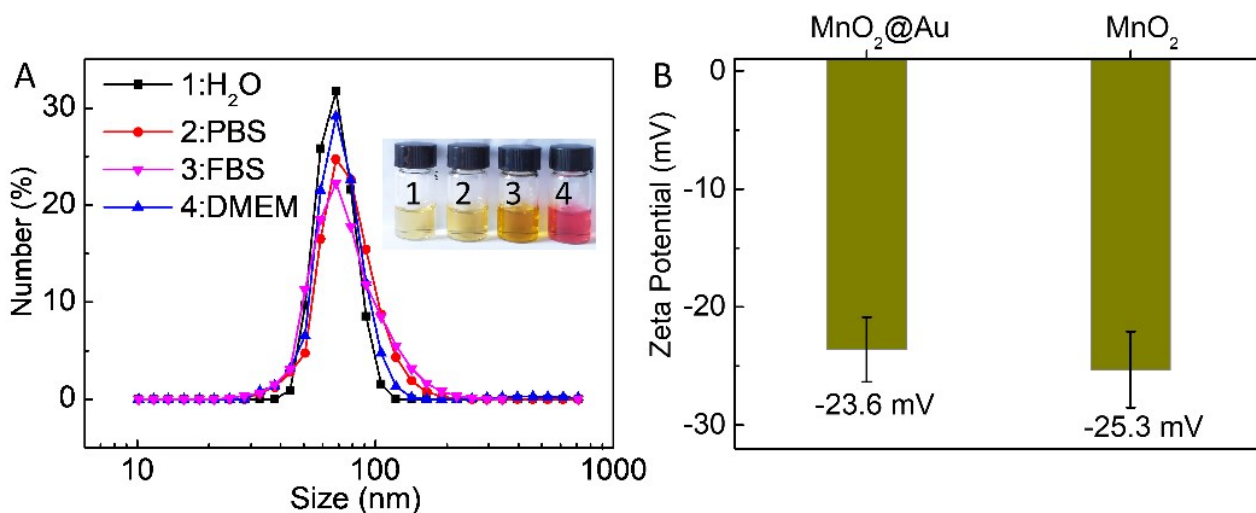
Fig. S6 (A) Hydrodynamic diameter distributions of MnO_2@Au NCs in H_2O, PBS, FBS and DMEM. Insets: a corresponding photograph of MnO_2@Au NCs in H_2O, PBS, FBS and DMEM. (B) Zeta potentials of MnO_2@Au NCs and MnO_2 NSs.

The obtained MnO_2@Au NCs demonstrated great colloidal stability in different physiological solutions, such as PBS, fetal bovine serum (FBS) and Dulbecco's modified Eagle's medium (DMEM), which is important for biomedical applications.
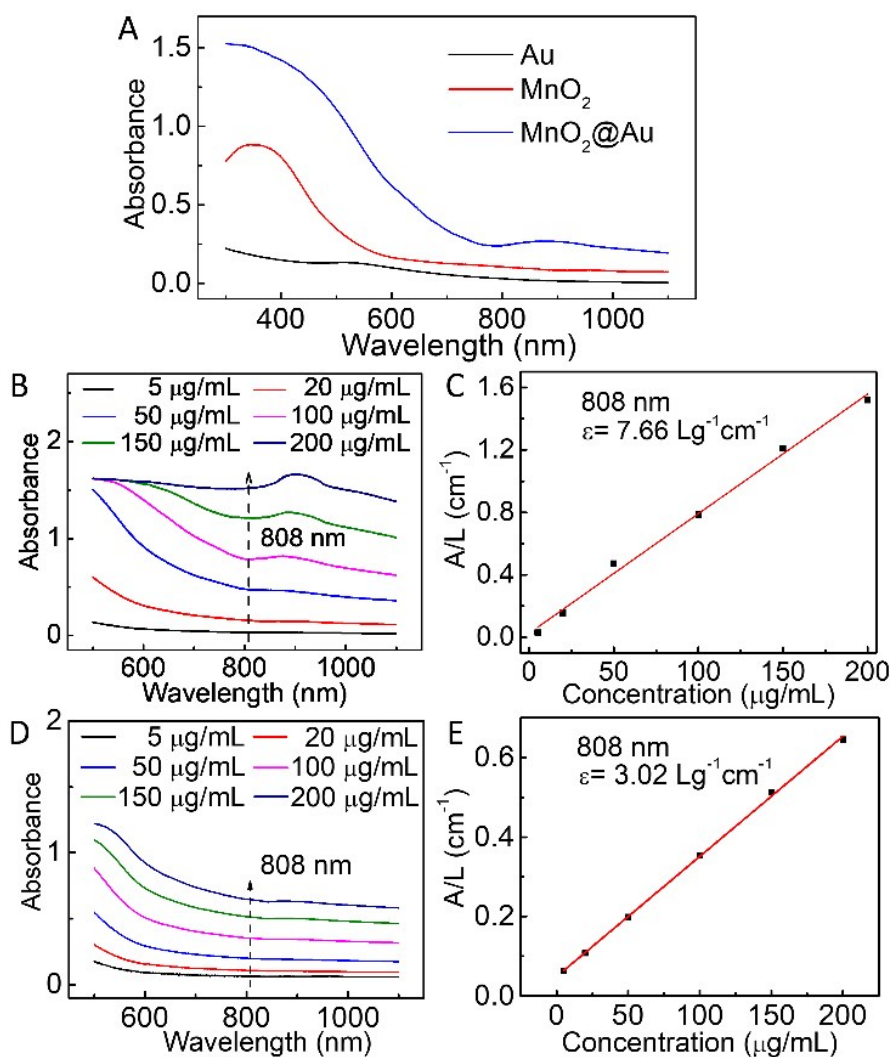
Fig. S7 (A) UV−vis spectra of Au NPs, MnO$_2$ NSs and MnO$_2$@Au NCs. UV−vis spectra of different concentrations of MnO$_2$@Au NCs (B) and MnO$_2$ NSs (D). Mass extinction coefficient of MnO$_2$@Au NCs (C) and MnO$_2$ NSs (E).

The mass extinction coefficient (ε) at 808 nm was measured to evaluate the light-absorption capability. Based on the Lambert–Beer law, the ε was calculated according to the following equation:

$A=\varepsilon LC$

A: the absorbance of materials at 808 nm

ε: the mass extinction coefficient (L g^{-1} cm^{-1})

L: the path length of 1 cm

C: the concentration of materials (μg/mL)

Then, we can obtain: $A/L=\varepsilon C$. The slope of A/L vs. concentration of C is the mass extinction coefficient of ε, which was estimated to be 7.66 L g^{-1} cm^{-1} and 3.02 L g^{-1} cm^{-1} for MnO$_2$@Au NCs and MnO$_2$ NSs, respectively.
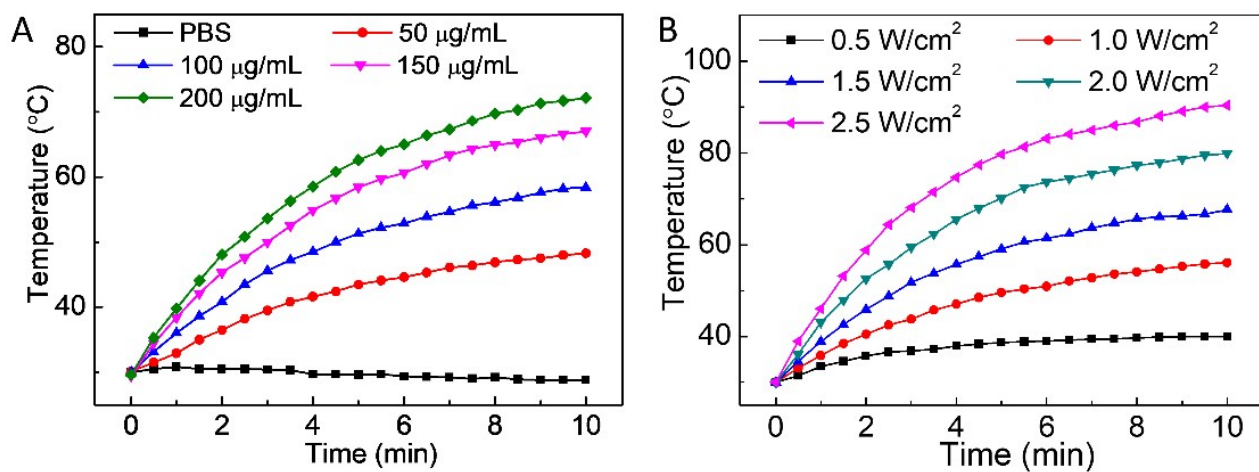
Fig. S8 Concentration- and laser power-dependent photothermal heating curves of $MnO_2@Au$ NCs.
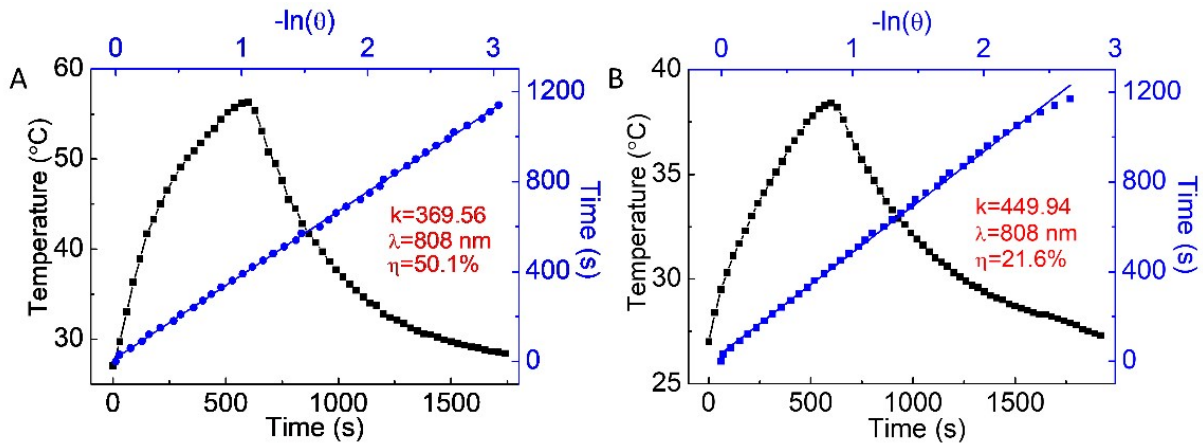
Fig. S9 Temperature rise and fall curves of MnO$_2$@Au NCs (A) and MnO$_2$ NSs (B), and linear time data versus −lnθ obtained from the cooling period.

The photothermal conversion efficiency (η) indicates the performance of agent in converting the light into heat. The η value was calculated by the following equation (1):

$$\eta = \frac{hA(T_{max} - T_0) - Q_0}{I(1 - 10^{-A_\lambda})} \times 100\% \qquad (1)$$

η: the photothermal conversion efficiency

h (mV/(m^2 °C)): the heat-transfer coefficient

A (m^2): the container's surface area.

T_{max} (°C): laser-irradiated maximum temperature of 56.3 °C and 38.43 °C for MnO$_2$@Au and MnO$_2$.

T_0 (°C): the ambient temperature of 27 °C.

Q_0 (mW): the heat energy caused by the light absorbing of the container and solvent, and is measured independently to be 20.0 mW.

I: the laser power of 1.0 W/cm^2.

A_λ: the absorbance of MnO$_2$@Au and MnO$_2$ at 808 nm of 0.787 and 0.353.

The value of hA can be calculated by the following equation (2):

$$hA = \frac{m_sC_s + m_wC_w}{k} \qquad (2)$$

m_s (g): the mass of the sample solution of 1.0 g.

C_s (J/(g K)): the sample heat capacity of 4.2 J/(g K).

m_w (g): the container mass of 1.0 g.

C_w (J/(g K)): the container heat capacity of 1.34 J/(g K).

k: the slope of the linear equation from cooling period vs −lnθ of 369.56 and 449.94 for MnO$_2$@Au

and MnO_2 (Fig. S9).

$$MnO_2@Au: \quad hA = \frac{1.0 \times 4.2 + 1.0 \times 1.34}{369.56} = 0.015 \tag{3}$$

$$MnO_2: \quad hA = \frac{1.0 \times 4.2 + 1.0 \times 1.34}{449.94} = 0.0123 \tag{4}$$

Finally, substituting hA value into Equation (1), the η can be calculated as following:

$$MnO_2@Au: \quad \eta = \frac{0.015 \times (56.3 - 27) - 0.02}{1.0 \times (1 - 10^{-0.787})} \times 100\% = 50.1\% \tag{5}$$

$$MnO_2: \quad \eta = \frac{0.0123 \times (38.4 - 27) - 0.02}{1.0 \times (1 - 10^{-0.3532})} \times 100\% = 21.6\% \tag{6}$$
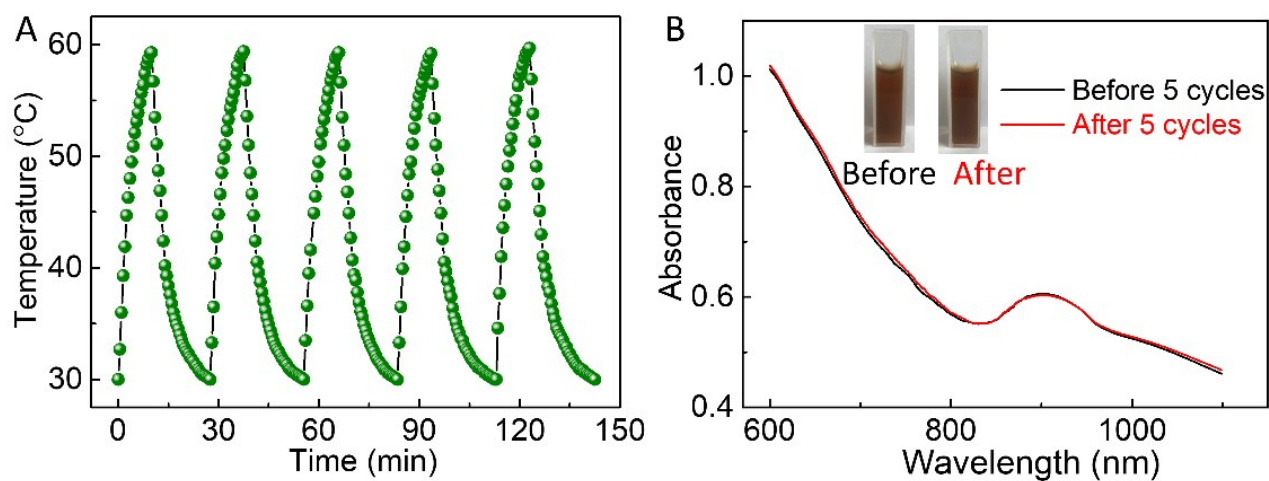
Fig. S10 (A) Heating curves of MnO_2@Au NCs suspension (100 μg/mL) for five laser on/off cycles. (B) Absorbance spectra of MnO_2@Au NCs before and after five laser on/off cycles.
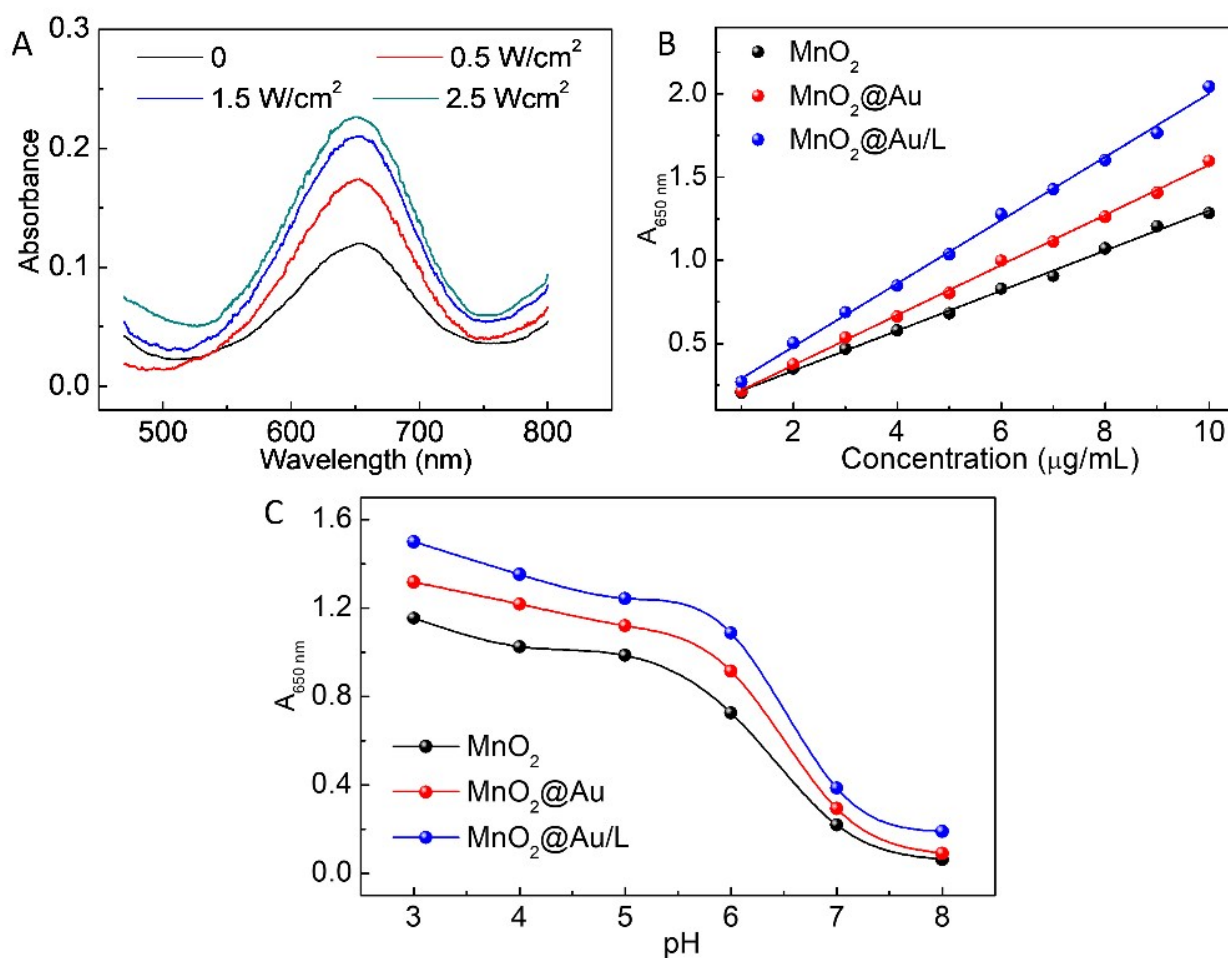
Fig. S11 (A) Absorbance spectra of TMB oxidization catalyzed by $MnO_2@Au$ with different power density of laser irradiation. (B) The concentration-dependent absorbance changes at 650 nm of TMB oxidation catalyzed by MnO_2, $MnO_2@Au$ and $MnO_2@Au/L$. (C) The pH influence for TMB oxidation catalyzed by MnO_2, $MnO_2@Au$ and $MnO_2@Au/L$.
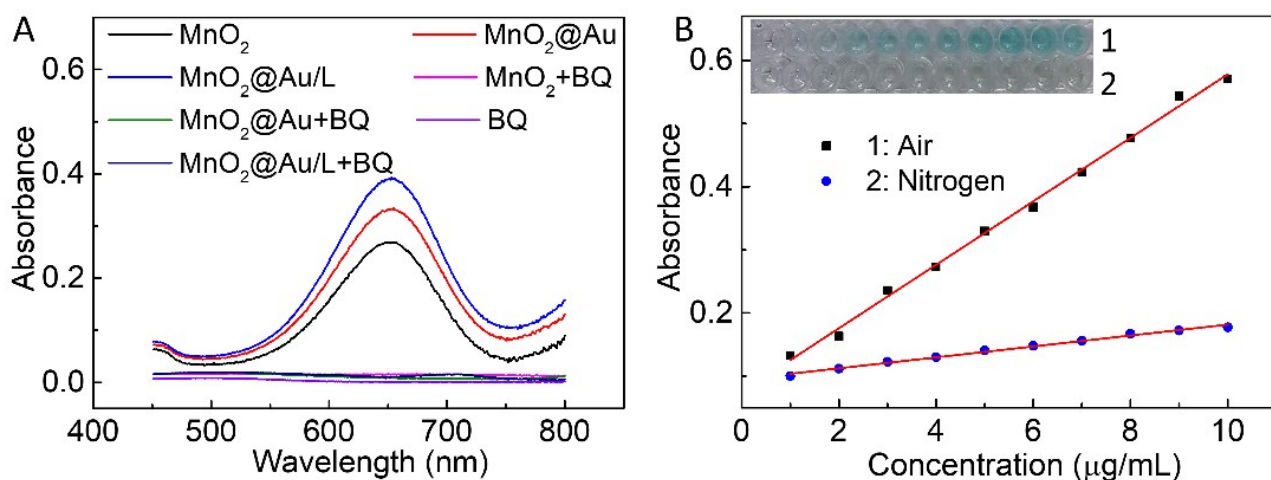
Fig. S12 (A) Absorbance spectra of TMB oxidization catalyzed by MnO_2, MnO_2@Au and MnO_2@Au/L in absence or presence of BQ. (B) The concentration-dependent absorbance changes at 650 nm of TMB oxidation catalyzed by MnO_2@Au with or without oxygen.
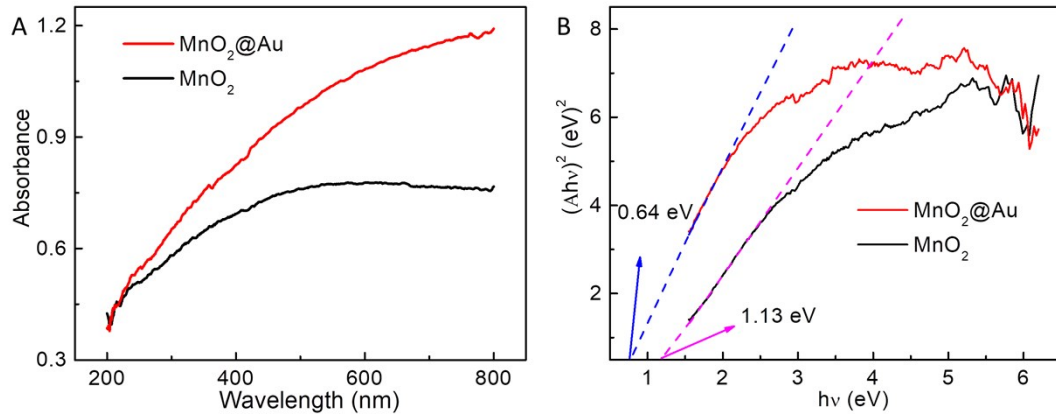
Fig. S13 UV-vis DRS (A) and the plotting of $(Ahv)^2$ vs. photon energy (B) of MnO_2@Au and MnO_2.

In order to obtain the band gap values, the following formula is adopted:

$\alpha hv = B(hv - E_g)^{m/2}$ (1)

α: molar absorption coefficient;

h: planck coefficient;

v: photon frequency;

B: proportional constant;

E_g: the band gap;

m: the value is related to semiconductor materials and transition types:

The value of m is 1 since MnO_2 is a kind of indirect semiconductor.

$\alpha hv = B(hv - E_g)^{1/2}$ (2)

According to Lambert's law, $A = \alpha bc$ (3)

A: the absorbance of sample;

α: molar absorption coefficient;

b: the thickness of sample;

c: the concentration of sample.

The value of α can be calculated by the following equation: $\alpha = A/bc$ (4)

Substitute α value into equation (2):

$Ahv/bc = B(hv - E_g)^{1/2}$ (5)

$(Ahv)^2 = (Bbc)^2(hv - E_g)$ (6)

Thus, the band gap values of semiconductors could be estimated from a plot of $(Ahv)^2$ vs the photon energy of hv. As shown in Fig. S13B, the band gap values of MnO_2@Au and MnO_2 were 0.64 and 1.13 eV, respectively.
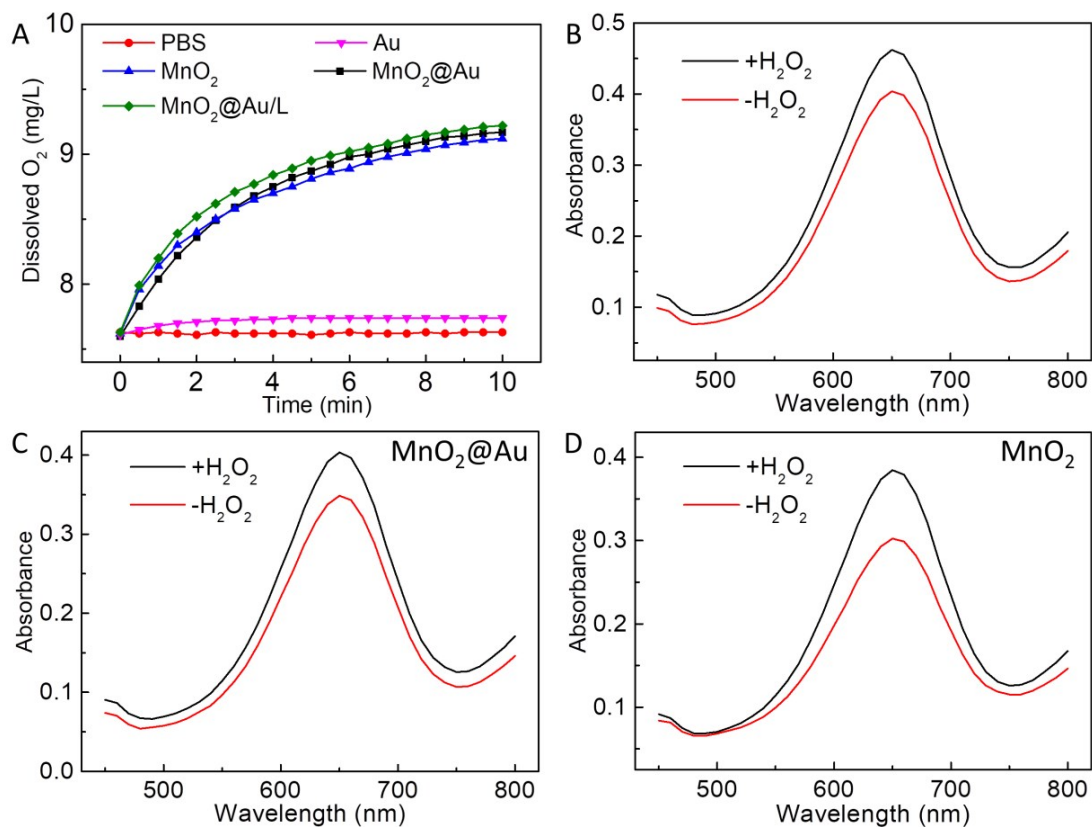
Fig. S14 (A) O_2 generation profiles in PBS, Au, MnO_2, MnO_2@Au and MnO_2@Au/L solutions with 100 μM of H_2O_2. Absorbance spectra of TMB oxidization catalyzed by MnO_2@Au/L (B), MnO_2@Au (C) and MnO_2 (D) in absence or presence of H_2O_2.
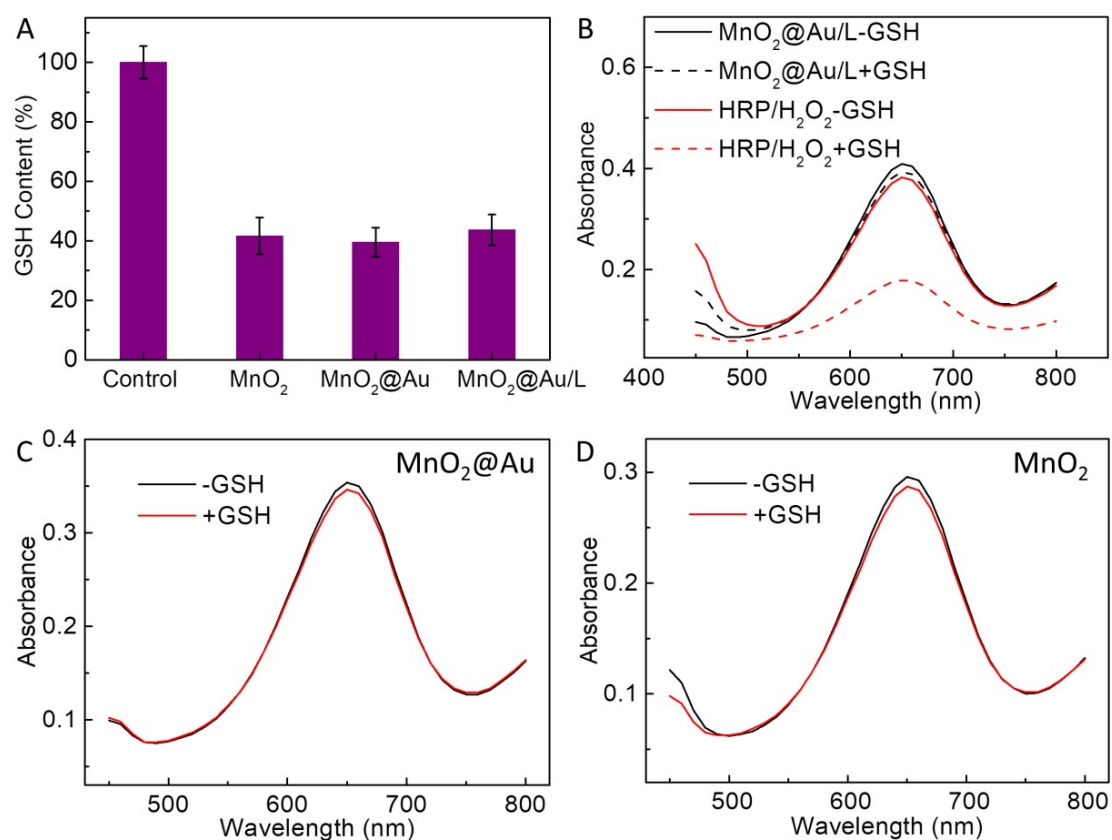
Fig. S15 (A) Relative content of GSH with or without MnO_2, MnO_2@Au and MnO_2@Au/L. Absorbance spectra of TMB oxidization catalyzed by MnO_2@Au/L or HRP/H_2O_2 (B), MnO_2@Au (C) and MnO_2 (D) in absence or presence of GSH.

Meanwhile, GSH-depleting capability of MnO_2-based nanomaterials was investigated by using 5, 5'-dithiobis-(2-nitrobenzoic acid) (DTNB) as indicator, which can react with GSH generating a new absorption at 410 nm.
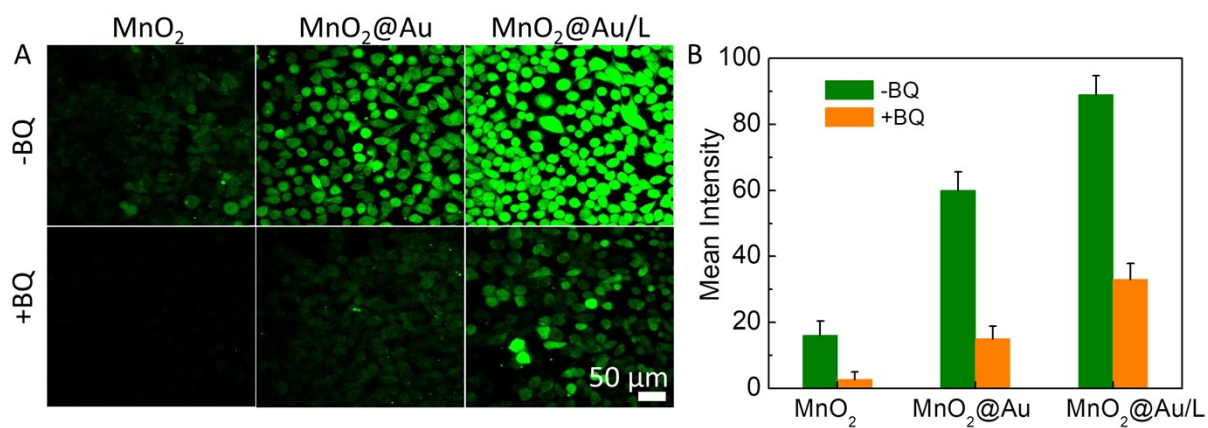
Fig. S16 (A) CLSM images of DCFH-DA in cells treated with MnO_2, MnO_2@Au and MnO_2@Au/L in the absence or presence of BQ. (B) Relative fluorescence intensities of Fig. S16A.
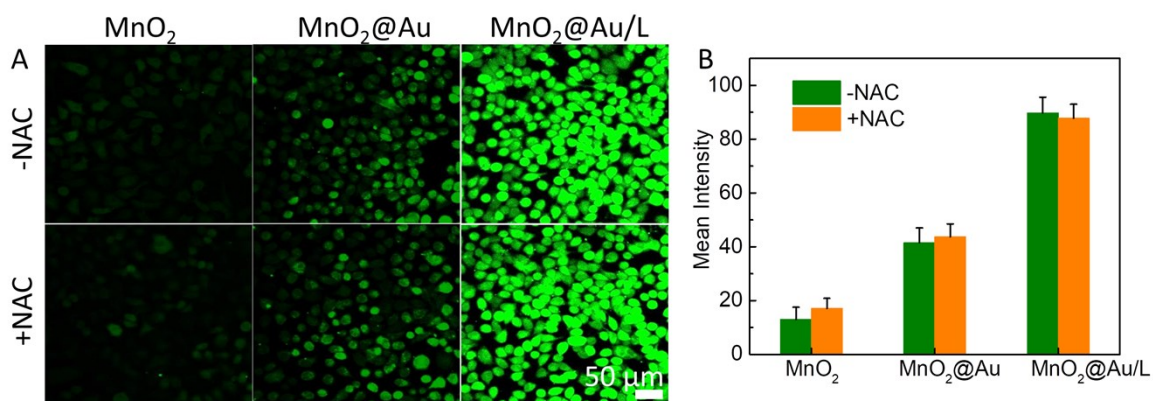
Fig. S17 (A) CLSM images of DCFH-DA in cells treated with MnO$_2$, MnO$_2$@Au and MnO$_2$@Au/L in the absence or presence of NAC. (B) Relative fluorescence intensities of Fig. S17A.

Indeed, no significantly reduced fluorescence intensity of DCFH-DA can be observed in GSH promoter (N-acetyl-L-cysteine, NAC)-pretreated cells, indicating an impaired antioxidation capability of MnO$_2$-based nanomaterials.
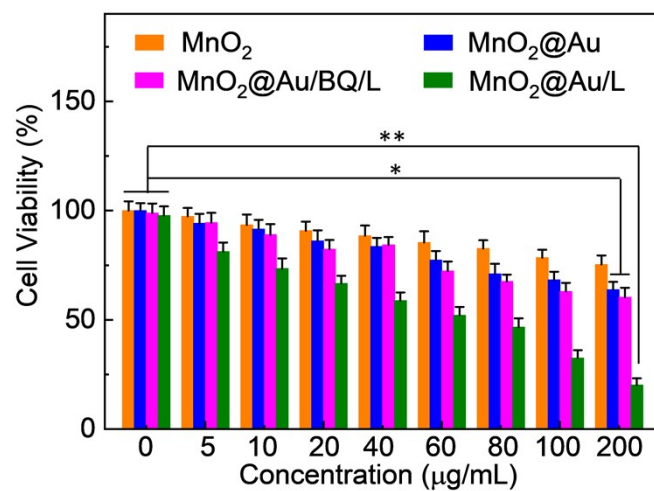
Fig. S18 The concentration-dependent cell viability of HeLa cells after different treatments for 24 h. Statistical significance is determined by Student's *t* test. *$p < 0.05$, **$p < 0.01$, ***$p < 0.001$.
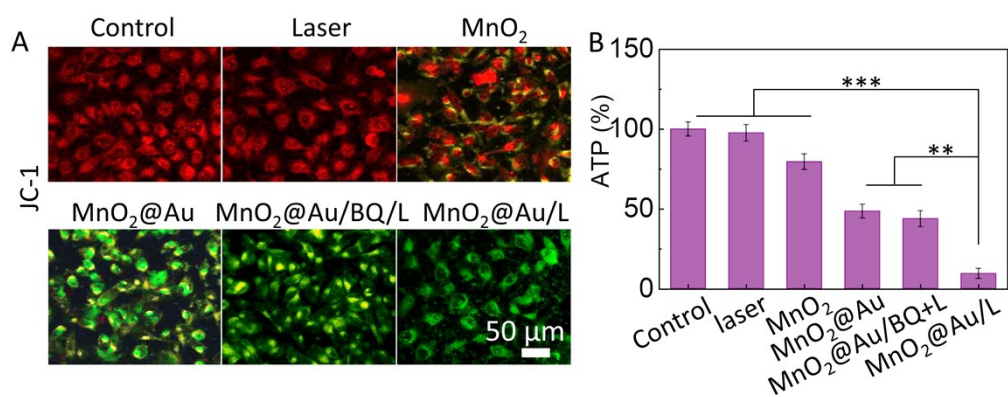
Fig. S19 (A) CLSM images of HeLa cells stained with JC-1 after different treatments. (B) The intracellular ATP level after different treatments. Statistical significance is determined by Student's t test. $*p < 0.05$, $**p < 0.01$, $***p < 0.001$.
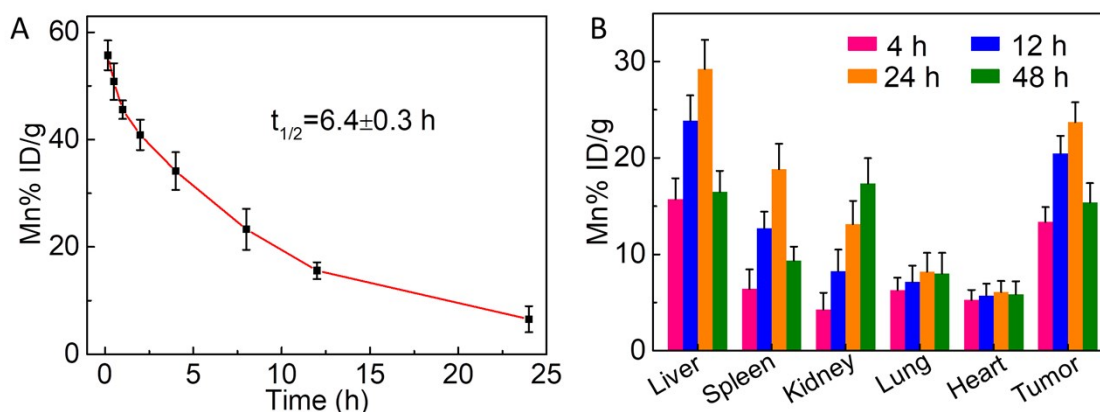
Fig. S20 Blood circulation curves (A) and time-dependent tissue distributions (B) of Mn concentration after intravenously injected of MnO_2@Au NCs in U14 tumour-bearing mice.

As shown in Fig. S20B, the MnO_2@Au NCs are dominantly accumulated in the spleen and liver due to high capture of the reticuloendothelial system (RES). Moreover, the Mn levels showed a time-dependent increase at tumour site following the maximum accumulation at 24 h postinjection. However, the Mn content gradually decreased in major organs except kidney, as the result of kidney clearance, thereby minimizing the long-term potential toxicity of MnO_2 @ Au NCs. Therefore, the laser irradiation was performed at 24 h postinjection to maximize the therapeutic effect.
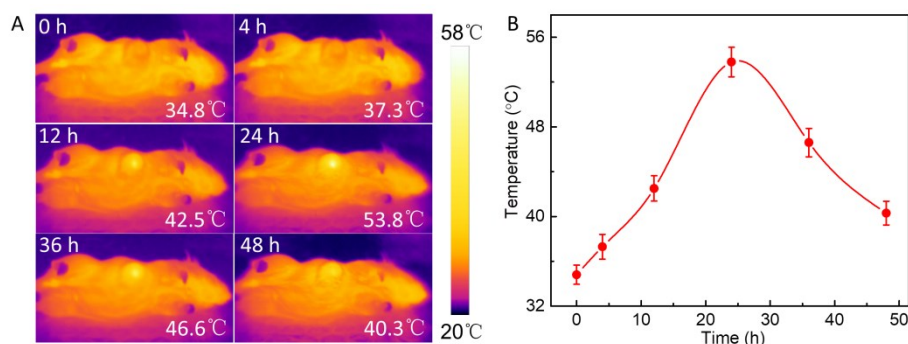
Fig. S21 *In vivo* thermal images (A) and tumour temperature variation (B) of tumour-bearing mice at 0, 4, 12, 24, 36, and 48 h postinjection of MnO_2@Au NCs with an 808 nm laser irradiation (1 W/cm^2, 10 min).

In vivo thermal images of tumour-bearing mice at 0, 4, 12, 24, 36, and 48 h postinjection of MnO_2@Au NCs were shown in Fig. S21. In the initial stage, the tumour site temperature gradually increased and reached maximum value of 53.8 °C at 24 h postinjection of MnO_2@Au NCs, and then the temperature gradually decreased despite the extended injection time as a result of clearance of the nanoparticles, which is well agreed with the time-dependent biodistribution results of MnO_2@Au NCs at main organs (Fig. S20B). Therefore, the MnO_2@Au NCs can reach optimal accumulation in tumour tissue at 24 h after the intravenous injection to maximize the therapeutic effect.
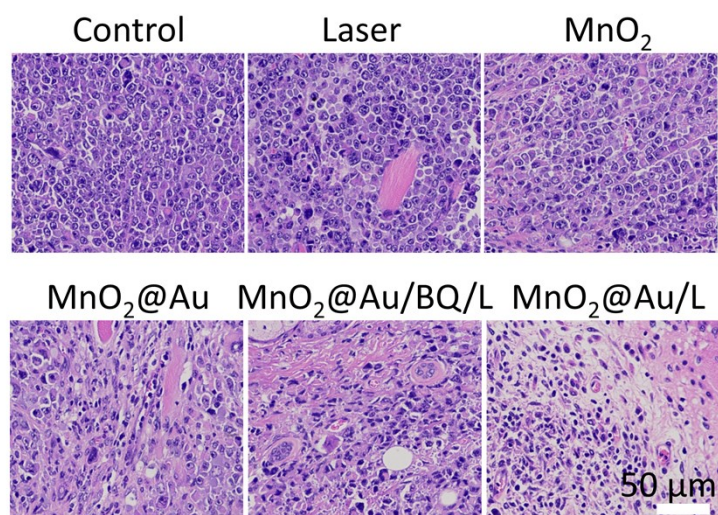
Fig. S22 Tumour H&E staining of mice after treatments.
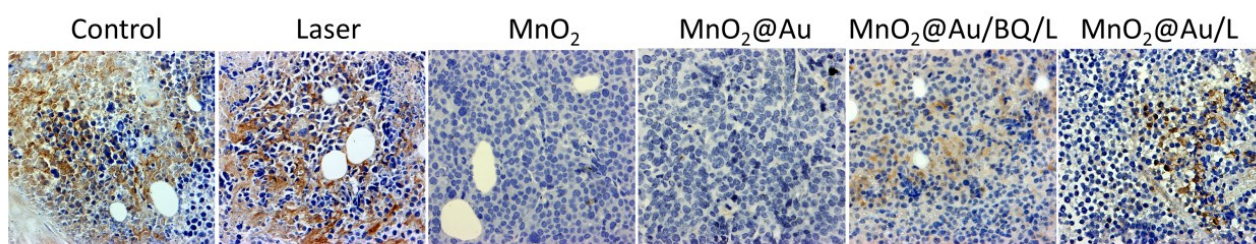
Fig. S23. Tumour HIF-1α staining of mice after treatments.

As can be seen in Fig. S23, the tumour cells in control and laser irradiation groups were stained dark brown due to the accumulation of HIF-1α under hypoxic condition. For MnO_2 and $MnO_2@Au$ groups, the tumour cells were stained blue, indicating that the tumours' hypoxic environment was alleviated by O_2 generation from the degradation of H_2O_2 in the presence of MnO_2-based nanomaterials. However, tumours were treated with either $MnO_2@Au/BQ/L$ or $MnO_2@Au/L$, and slight up-regulation of HIF-1α expression was observed in brown color because partial O_2 can be converted to highly toxic $\cdot O_2^-$. Thus, the results demonstrated that the $MnO_2@Au$ NCs successfully relieved the tumour hypoxia, leading to improved tumour oxygenation, which was expected to be favorable for the enhancement of subsequent O_2-dependent ROS therapy efficiency.
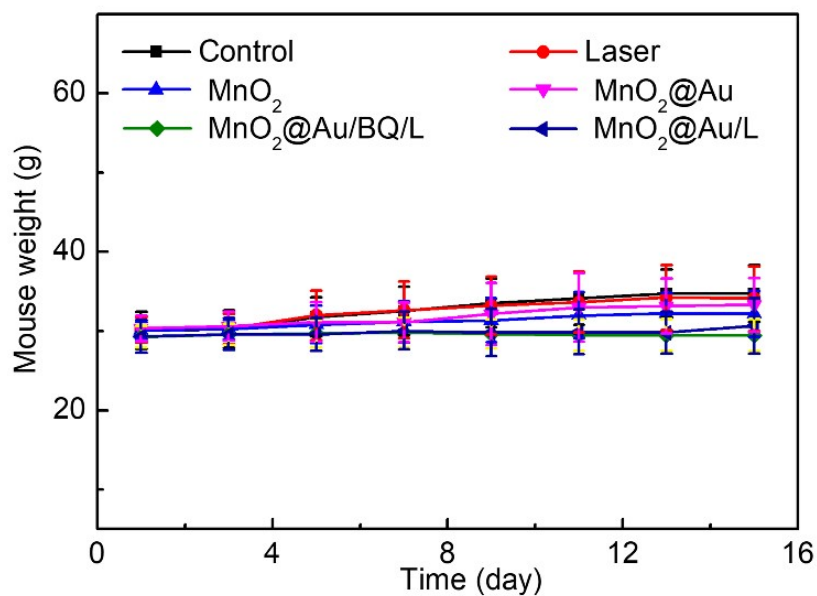
Fig. S24 Time-dependent body-weight curves of mice in various treatment groups.

No remarkable body weight drop was caused in all the experimental groups (Fig. S24), confirming low systemic side effects of MnO_2-based materials in blood circulation system due to the low ROS efficiency at neutral conditions.
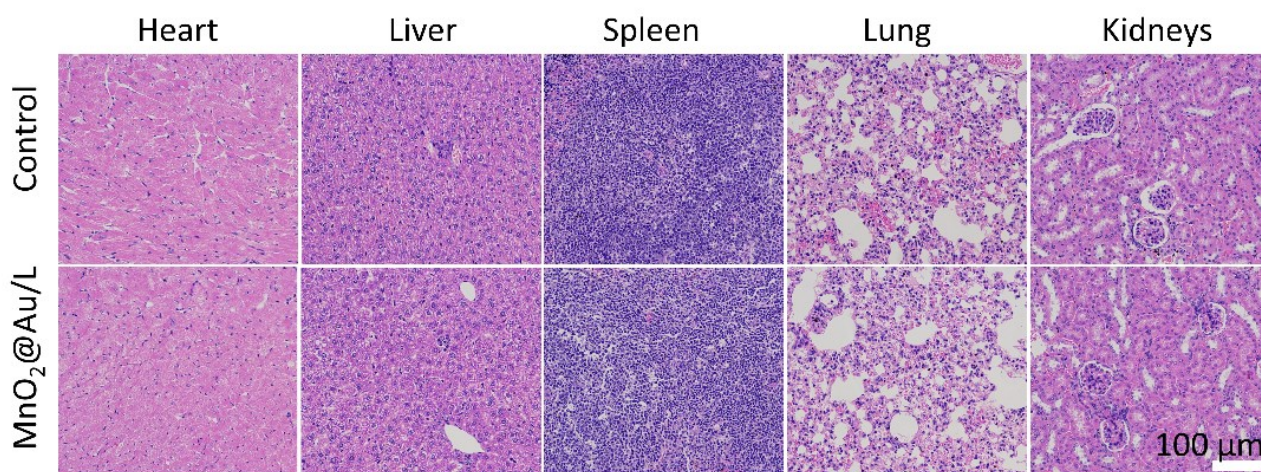
Fig. S25 H&E staining of major organs from mice treated with or without MnO$_2$@Au/L.

The low systemic toxicity of MnO$_2$@Au was further evaluated through HE staining analysis. No obvious tissue impairment was observed by H&E staining, further confirming low side effects and high biosafety of MnO$_2$@Au.

References

1. L. Yan, L. Niu, C. S., Z. Zhang, J. Lin, F. Shen, Y. Gong, C. Li, X. Liu, Shiqing Xu, *Electrochim. Acta*, 2019, **306**, 529-540.

2. Y. Zhao, C. Chang, F. Teng, Y. Zhao, G. Chen, R. Shi, G. Waterhouse, W. Huang, T. Zhang, *Adv. Energy Mater.*, 2017, **7**, 1700005.

3. X. Zhou, P. L. Burn, B. J. Powell, *Inorg. Chem.*, 2016, **55**, 11, 5266–5273.